
RISING A NEW FRAMEWORK FOR FEW-VIEW TOMOGRAPHIC IMAGE RECONSTRUCTION WITH DEEP LEARNING

A PREPRINT

Davide Evangelista

Department of Mathematics
University of Bologna, Italy
davide.evangelista5@unibo.it

Elena Morotti

Department of Political and Social Sciences
University of Bologna, Italy
elena.morotti4@unibo.it

Elena Loli Piccolomini

Department of Computer Science and Engineering
University of Bologna, Italy
elena.loli@unibo.it

January 25, 2022

ABSTRACT

This paper proposes a new two-step procedure for sparse-view tomographic image reconstruction. It is called RISING, since it combines an early-stopped Rapid Iterative Solver with a subsequent Iteration Network-based Gaining step. So far, regularized iterative methods have widely been used for X-ray computed tomography image reconstruction from low-sampled data, since they converge to a sparse solution in a suitable domain, as upheld by the Compressed Sensing theory. Unfortunately, their use is practically limited by their high computational cost which imposes to perform only a few iterations in the available time for clinical exams. Data-driven methods, using neural networks to post-process a coarse and noisy image obtained from geometrical algorithms, have been recently studied and appreciated for both their computational speed and accurate reconstructions. However, there is no evidence, neither theoretically nor numerically, that neural networks based algorithms solve the mathematical inverse problem modelling the tomographic reconstruction process. In our two-step approach, the first phase executes very few iterations of a regularized model-based algorithm whereas the second step completes the missing iterations by means of a neural network. The resulting hybrid deep-variational framework preserves the convergence properties of the iterative method and, at the same time, it exploits the computational speed and flexibility of a data-driven approach. Experiments performed on a simulated and a real data set confirm the numerical and visual accuracy of the reconstructed RISING images in short computational times.

Keywords Deep Learning · Convolutional Neural Network · Model-based iterative solver · Sparse-view tomography · Tomographic imaging

1 Introduction

Combining healthy protocols with high quality images is one of the most important component of medical imaging and a crucial target for researchers involved in minimal invasive Computed Tomography (CT). Radiologists, manufacturers and medical physicists have implemented many examination protocols as well as software and hardware modifications to reduce the harmful ionizing radiations and pave the way to X-ray examinations for screening tests, pediatric cases, or pre-surgical examinations. There are two main techniques allowing for a significant reduction of the total radiation exposure per patient. The first one consists in reducing the X-ray tube current at each scan, without changing the full geometry traditionally used in CT (*low-dose CT*). The measurement data are very noisy due to the excessive quantum

noise. The second practical way to lower the radiation per person consists in reducing the number of X-ray projections (*few-view CT*), which leads to incomplete tomographic data, but very fast examinations.

In this paper, we focus on few-view CT images, whose reconstruction is tricky: the lack of projections makes the discrete inverse problem mathematically modelling the reconstruction phase have infinite possible solutions [1]. Conventional filtered backprojection (FBP) algorithms, widely exploited in classical CT, do not provide stable reconstructions as the Tuy-Smith condition is not satisfied [2], and the recovered images suffer from severe striking artifacts.

A widely used alternative approach is represented by model-based iterative methods. They model the image reconstruction as a mathematical linear inverse problem which is solved, in the discrete setting, by minimizing a constrained or unconstrained function combining a data-fit term and a regularizer. The embedding of a sparsifying regularizer mitigates the lack of many angled views, according to the Compressed Sensing (CS) theory [3]. However, the resulting iterative schemes solving the minimization problem are still computationally expensive and typically need several iterations to achieve high quality results. An exhaustive review of model-based reconstruction methods can be found in [4].

Recently, Deep Learning (DL) based methods have emerged over fully conventional or variational approaches for few-view tomographic reconstruction [5]. The two widely used strategies consist in unrolled methods, which mimic the implementation of an iterative reconstruction algorithm through network layers, and the so called Learnt Post Processing (LPP) approach. In particular, the LPP is a two-step scheme where first a low quality image with artifacts and noise is reconstructed with a fast method (typically a FBP) and then a neural network suppresses the artifacts. Usually, the network learns from a set of *ground truth* images reconstructed from full dose acquisitions. The pioneering works by Han demonstrated in 2016 and 2018 the superiority of LPP strategies over some model-based iterative algorithms for sparse-view CT images [6, 7]. However, in their inspiring work [8], Sidky et al. claim that the popular LPP schemes lack of mathematical characterization.

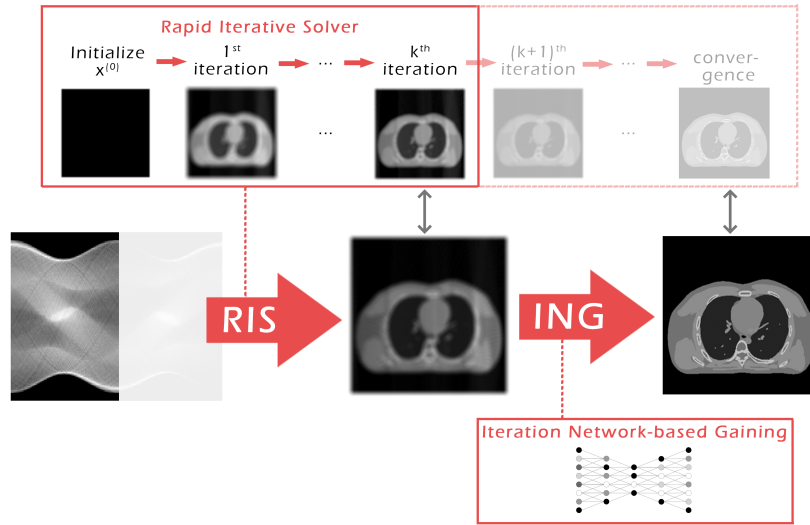


Figure 1: Graphical draft of the proposed two-step RISING workflow for tomographic reconstruction from sparse-view data.

Motivations. The main disadvantage of model-based iterative reconstruction algorithms is their high computational cost. On real systems, in order to fulfill the clinical requirements of time per exams, only very few iterations of the algorithms can be performed, leading to a solution which is not the best one. However, by considering fast iterative methods, the images reconstructed in few iterations already contains many details of interest of the scanned object [9, 10].

Focusing on data-driven methods based on deep learning, the work by Sidky et al. [8] claims and demonstrates that LPP schemes do not compute the solution of the CT inverse problem and they can introduce structures not belonging to the scanned objects in the reconstructions. On the contrary, numerical evidence shows that model-based methods compute a good solution of the inverse problem, in the sense that will be defined in the next section. In addition, it is worth notice that the efficiency of the deep learning based methods strictly depends on the training phase and, above all for CT applications, on the training samples. In fact, neural networks need to be trained on task-specific data sets to properly learn both the degradation effects to remove and the anatomical details to preserve characterizing each topology of medical imaging, and a further relevant challenge for medical applications is the lack of precise training data [5]. To the best of our knowledge, in the state-of-art literature the neural networks are always trained on ground

truth images, achieved with full-dose CT protocols, hence we argue that such projection measurements may be not achievable in some CT applications (for instance, where physical constraints prevents the full-range acquisition, as in limited-angle protocols).

Contribution. Strong of this awareness, this paper proposes a new hybrid iterative and data-driven scheme for the resolution of the sparse-sampling CT inverse problem.

This work has a dual purpose. On one side, we aim at computing a suitable solution of the inverse tomographic reconstruction problem as accurately as possible in a short computational time, consistent with the clinical requirements. On the other side, we intend to remedy to the lack of task-specific CT data sets by using, for networks training, images created by the same system and under the same geometry used for the reconstruction. This is attainable for every CT system.

To achieve our purposes, we propose to apply a model-based iterative method and speed up the approaching to convergence with a neural network trained on accurate task-specific images achieved by few-view protocols.

Proposal. We refer to our proposal as the *RISING* (Rapid Iterative Solver with Iteration Network-based Gaining) framework. *RISING* is conceived as the reconstructing procedure, described by the two following steps executed in sequence:

- Starting from the subsampled projection data, a rapid iterative algorithm produces a preliminary coarse reconstruction, by solving the model-based problem handling few-view CT with a few iterations. The execution of only few iterations fits realistic time constraints.
- The previously computed rough reconstruction is processed by a deep neural network which aims at retrieving the unperformed iterations towards the convergence. Its output is the *RISING* solution image. As the execution of a neural network is very fast, the use of DL in this step greatly speed-ups the whole reconstruction. Differently from other DL-based schemes, in *RISING* the network is trained on target images obtained offline as solutions of iterative solver at convergence, from projection data acquired under the CT geometry in exam. This ensures a fully consistent training to all types of medical images and sparse-view protocols.

A graphical draft of *RISING* is depicted in Figure 1.

To validate our proposal, we apply the *RISING* approach on real and synthetic CT data sets simulating various sparse-view settings. In all the cases, we achieve high quality reconstructions and the quality measures on the synthetic data set confirm that the results are reliable solutions of the CT inverse problem. We developed our *RISING* workflow in Python and the code is available at <https://github.com/loibo/RISING>.

Organization of the paper. The paper is organized as follows. In Section 2 we state the CT inverse problem and present the state-of-art DL-based methods addressing it, then Section 3 describes the proposed *RISING* framework. In Section 4 we introduce the experimental settings considered to achieve the results reported and discussed in Section 5. At last, final conclusions are drawn in Section 6.

2 Few-view X-ray CT image reconstruction methods

It is well known that the tomographic acquisition can be modelled as a linear process where the projections are obtained by applying the Radon transform to the object [11].

For simplicity, we consider in this paper the model discretization in two dimensions. The extension to three dimensions is straightforward.

In discrete setting, the CT process of X-ray absorption is expressed as:

$$Ax = b \tag{1}$$

where the unknown vector $x \in \mathbb{R}^{n^2}$ denotes the image to reconstruct, the right-hand side term b is an m -dimensional vector containing the projection measurements and the $m \times n^2$ system matrix A is the discretization of the X-ray physical process projecting an $n \times n$ image onto the detector. We say that an inverse problem is *solvable* in a subset Ω if it admits a unique solution in Ω .

In case of few-view CT protocols, equation (1) is not solvable in \mathbb{R}^{n^2} , since the under-determined linear system admits infinite solutions (recalling that $m < n^2$). According to the Compressed Sensing (CS) theory [3], if the desired solution x^* of (1) is sparse in some transform Tx , then (1) is solvable in the subset $\Omega = \{x \in \mathbb{R}^{n^2} \mid \|Tx\|_0 \leq d\}$, where $\|\cdot\|_0$

is the ℓ_0 semi-norm counting the non-zero elements of the vector argument. Hence the CT inverse problem can be reformulated as the following minimization:

$$x^* = \arg \min_x \|Tx\|_0 \text{ s.t. } Ax = b. \quad (2)$$

Since equation (2) is difficult to solve numerically, it is usually relaxed as:

$$\arg \min_x \|Tx\|_1 \text{ s.t. } Ax = b, \quad (3)$$

where $\|\cdot\|_1$ is the ℓ_1 norm [12]. An unconstrained formulation of (3) can be stated as:

$$\arg \min_x \|Ax - b\|_2^2 + \lambda \|Tx\|_1 \quad (4)$$

where λ is a suitable positive parameter (also called *regularization parameter*). The resulting convex optimization problem can be solved by convergent iterative methods such as the lagged diffusivity fixed point algorithm [13] or FISTA [14]. Usually, the constraint $x \geq 0$ is added in (3) or (4), to preserve the physical the non-negativity properties of the attenuation coefficients [15, 16, 10].

Deep methods for CT reconstruction

As anticipated, algorithms exploiting deep Convolutional Neural Networks (CNNs) have been proposed for few-view CT image reconstruction for few years. Many publications have focused on learning iterative schemes through *unrolling* (or unfolding) strategies, where a model-based iterative solver is unfolded into the sequence of its iterations [17]. Since each iteration of the unrolled methods matches the computations performed in the correspondent iteration of the model-based algorithm, these methods aim at recovering the solution of the inverse problem through a minimization. However, they are trained on full dose images as targets, which differ from the inverse problem solution. Hence, there is no evidence that the reconstructed image well approximates the solution of the inverse tomographic problem. Moreover, the neural networks employed for unfolded schemes suffer from instabilities, such as vanishing gradient [18]. To reduce these unwanted effects only a limited number of unfolded iterations are performed, stopping the method far before convergence.

The proposals differ for the considered iterative scheme and for the block-per-iteration learnt by the neural network. We give a short overview of the most recent works. In [19], Adler and Oktem have developed a partially learned gradient descent algorithm, whereas they have worked on the Chambolle-Pock scheme in [20]. In [21] a CNN is trained to act like a projector in a gradient descent algorithms, while in [22], both the proximal operator and gradient operator (which correspond to A^T when it is applied to a problem corrupted with additive Gaussian noise) of an unrolled FISTA scheme are learned, whereas in [23] the neural network learns the initial iterate of the inner Conjugate Gradients solver in a splitting scheme for optimization.

A completely different data-driven proposal for CT image reconstruction is represented by the *Learnt Post-Processing* (LPP) approach. It consists in a two-step framework where, firstly, a fast reconstruction algorithm is applied off-line to compute the medical image from the projection data, then a learnt neural network is applied as post-processing operator to restore the low-quality image. It is worth notice that most of the networks used for LPP are applied to corrupted images provided by the FBP solver (see for example [7, 24, 25, 26, 27, 28] and the references therein). Only in [29] and in [30] the preliminary solutions are computed by wavelet- or TV-based iterative solvers, respectively.

Model-based vs LPP methods. In addition, the seminal paper [8] has found out an important observation addressing LPP schemes in comparison to CS model-based approaches. Indeed, CS theory has not provided analytic results for X-ray CT measures, hence the authors have considered a set of digital breast phantoms and built CT simulations. When considering as ground truth test images characterized by sparse gradient domains, the tests confirmed that the solution of problem (3) computed by a regularized CS based iterative method is very close to the true solution. On the contrary, the LPP framework produces worse performances, showing that the network is not able to solve the inverse problem.

3 The proposed RISING framework

In this section, we describe the proposed new framework. It is denoted as RISING since it combines a Rapid Iterative Solver (RIS) phase with a following Iteration Network-based Gaining (ING) phase. The RISING workflow is also graphically depicted in Figure 1.

Briefly, we look for a sparse solution in a gradient domain and we apply an iterative model-based algorithm to a minimization model such as (3). Instead of getting the algorithm solution at convergence, we perform only a predefined

(and relatively small) number K of iterations and stop the solving algorithm before its convergence, to meet the constraints imposed by clinical setting where very short computational time are admitted to the reconstruction process. The resulting early output represents the input of the neural network which enhances the image in a new perspective, trying to retrieve the unperformed iterations instead of executing a LPP.

3.1 Rapid Iterative Solver

The first step of the RISING framework implements the Rapid Iterative Solver (RIS) to the following minimization problem:

$$\arg \min_{x \geq 0} \|Ax - b\|_2^2 + \lambda TV_\beta(x) \quad (5)$$

where, in order to have a differentiable objective function, we consider the smoothed version of the Total Variation (TV) [31] operator defined as:

$$TV_\beta(x) = \sum_{j=1}^{n^2} \sqrt{\|\nabla x_j\|_2^2 + \beta^2} \quad (6)$$

with β fixed small positive parameter.

Among the wide class of iterative solvers for the problem (5), we select the Scaled Gradient Projection (SGP) algorithm, proposed in 2008 for image deblurring [32]. The SGP has been successfully applied with some acceleration techniques for few-view CT reconstructions [33, 9, 10], where the authors show that the objects of interest are distinguishable in the solution obtained after very few iterations of the method. Regarding the convergence, it is proved in [34] that the theoretical convergence rate of the SGP at the unique minimum of (4) is $\mathcal{O}(1/k)$; they also numerically show that the practical performance of SGP method is very well comparable with the convergence rate of the optimal algorithms. For a detailed presentation of SGP method in tomographic imaging see [33].

In RISING, we stop the execution of the Iterative Solver at a prefixed iteration K , far before the numerical convergence, and the early solution $x^{(K)}$ is denoted as x_{RIS} in the following. From our previous works [33, 9] we know that, due to the empirical rapidity of the SGP, in the achieved coarse image reconstruction the anatomical structures are present but typically very blurred and weakly evident.

3.2 Iteration Network-based Gaining

The second step of the RISING framework implements the Iteration Network-based Gaining (ING) task. Here, a Convolutional Neural Network (CNN) learns the transformation mapping the early solution x_{RIS} , achieved in K iterations, to the corresponding convergence image computed in K^* iterations.

We denote with \mathcal{T}_j the function describing the action of the j -th iteration of the solver such as:

$$x^{(j+1)} = \mathcal{T}_j(x^{(j)}; b) \quad \forall j \geq 0.$$

Thus, the whole iterative process can be expressed as the concatenation of the following g_K and f_K functions:

$$g_K := \mathcal{T}_{K-1} \circ \cdots \circ \mathcal{T}_1 \circ \mathcal{T}_0 \quad (7)$$

and

$$f_K := \mathcal{T}_{K^*} \circ \cdots \circ \mathcal{T}_{K+1} \circ \mathcal{T}_K. \quad (8)$$

In fact, if we label the image achieved by the Iterative Solver at convergence as x_{IS} , it holds:

$$f_K(g_K(x^{(0)}; b)) = x_{IS}. \quad (9)$$

Since in the RIS step we compute $x_{RIS} = g_K(x^{(0)}; b)$, in the ING phase we need to recover f_K . To do so, we train a CNN to play as f_K when applied on x_{RIS} . Ideally, if the network would perfectly learn f_K , its output x_{ING} should be equal to x_{IS} . It is well known that this is not doable in practice; nevertheless, we show numerical evidence of our claims, through very accurate RISING reconstructions on simulations, in section 5.

We remark that, differently from the RISING approach, in case of LPP the CNN tries to learn an image-to-image relation which is not necessarily a function.

4 Experimental design and implementation notes

To numerically verify the feasibility of the RISING workflow, we develop numerical simulations. We consider real medical images, to properly understand the potential of RISING for clinical applications and settings, as well as a synthetic data set of images with geometric elements, where measures of merits can be computed.

This section describes the experimental design, whereas the results are reported and discussed in section 5.

4.1 Data set and test problems from real medical images

As real patient images, we have downloaded the widely used AAPM Low Dose CT Grand Challenge data set by the Mayo Clinic [35]. The considered images are 512×512 pixel reconstructions of human abdomen, computed from full-dose acquisitions. In Figure 2 we depict one image with two zooms-in highlighting areas with different anatomical structures, such as pulmonary details, sections of ribs and low-contrast inter-costal muscles. In all the experiments reported in 5.1, we have used the images from the data set as ground truth x_{GT} references. Coherently, we simulate the tomographic projections of the ground truth images, according to a 2D fan-beam geometry, and we add to the sinograms white Gaussian noise with 10^{-2} noise level. To address sparse-view CT reconstructions, we considered two different protocols: the first one is a full angular acquisition with 1-degree spaced projections (we call it $P_{360,360}$ in the following); in the second one the scanning trajectory covers 180 degrees and computed only 60 projections (it is labelled as $P_{180,60}$).

The RIS step executes only $K = 15$ iterations, hence we denote as $x_{RIS} = x^{(15)}$ the SGP output which is passed as input to the ING phase.

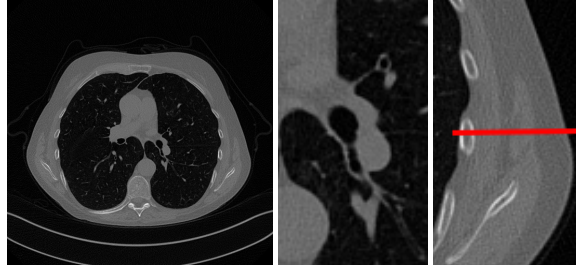


Figure 2: A ground-truth image from the Low Dose Mayo data set, with two zoomed crops on regions with different anatomical structures.

4.2 Data sets and test problems from synthetic images

As visible from Figure 2, real full-dose medical images still present little noise and slightly visible streaking artifacts. This makes quite difficult to compute reliable metrics on the reconstructions. To fully exploit the full-reference image quality assessment metrics and validate our experiments, we create synthetic images and build few-view CT simulations, whose results are analysed in 5.2. In particular, the Constrained Overlapping Uniform Lines and Ellipses (COULE) data set contains 430 sparse-gradient gray-scale images of 256×256 resolution with many overlying objects, varying in size and contrast with respect to the background. The left image of Figure 3 shows one image of the data set as an example. The whole data set is downloadable from www.kaggle.com/loiboresearchgroup/coule-dataset.

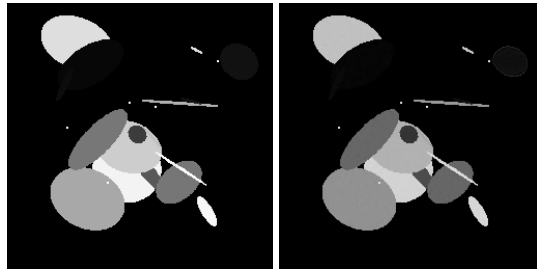


Figure 3: From left to right: ground-truth and x_{IS} reconstruction of an image from the COULE data set.

The simulations are computed as before. We consider now different RIS images, i.e. $x_{RIS} = x^{(3)}$, $x_{RIS} = x^{(5)}$ and $x_{RIS} = x^{(10)}$ for the $P_{360,360}$ setting. We also explore different geometries $P_{360,180}$ and $P_{360,60}$, by reducing the number acquired projections. On the right of Figure 3 we depict the SGP solution x_{IS} at convergence: we underline that it is visually not distinguishable from x_{GT} .

4.3 The Network architecture and its training

As CNN architecture we use the state-of-the-art ResUNet architecture. We exploit the pooling/unpooling strategies characterizing the popular U-net architecture by [36], because we need to approximate the complex image-to-image transformation f . Moreover, the addition of residual connections between the different levels of image resolution helps maintaining stable the training process and it has already been successfully applied to few-views CT image enhancement in [7, 37]. The activation function is *ReLU* for each layer, except for the latter where *tanh* is used instead.

With Mayo Clinic data set we select $N = 3306$ images (corresponding to 10 patients) for the training phase and 357 images (one patient) for testing. For the COULE data set, we use $N = 400$ images for training and 30 for testing.

Given the data set $\{(x_{RIS,i}, x_{IS,i})\}_{i=1,\dots,N}$, we denote by $F_{\theta^*}(x_{RIS,i})$ the action of the neural network on the input $x_{RIS,i}$ and by $x_{ING,i} = F_{\theta^*}(x_{RIS,i})$ the network output. We estimate by network training, where the loss function is set as $\ell(x_{IS,i}, x_{ING,i}) = \|x_{ING,i} - x_{IS,i}\|_2^2$, the parameters θ^* such that

$$\theta^* = \arg \min_{\theta} \frac{1}{N} \sum_{i=1}^N \ell(x_{IS,i}, x_{ING,i}). \quad (10)$$

The training is performed by running Adam for 50 and 100 epochs for the Mayo and COULE datasets, respectively. The batch size is fixed equal to 8 in all the experiments (this is the largest batch size usable in our Nvidia RTX A4000 GPU). The step size for the optimization algorithm decreases with polynomial decay, going from 10^{-3} to 10^{-5} . To increase the stability over the first iterations, we clip the gradient to 5.

4.4 Implementation notes

As already remarked in section 3.1, we use SGP as the iterative solver. In each iteration, we use the class *OpTomo* of Astra toolbox [38, 39] to compute the matrix-vector products Ax and $A^T y$, where A is the matrix in equation (1). We remark that *OpTomo* provides the exact transpose of the projector operator A for 2D tomography. In our experiments, we set the smoothing parameter for the TV regularizer to $\beta = 10^{-3}$, the regularization parameter as $\lambda = 1 \cdot 10^{-5}$ for the Mayo data set and $\lambda = 4 \cdot 10^{-5}$ for the COULE data set. All the SGP inner parameters are taken from [33].

4.5 Methods for comparisons

In our experiments, we compare the RISING reconstructions with respect to the image solutions x_{IS} achieved by the SGP solver at its numerical convergence, both to evaluate the visual improvements and to analyse the learnability of the iterations.

In addition, we also consider the images computed by first applying the same RIS step as before and then restoring the x_{RIS} image with a data-driven post-processing step. Here, we apply the same ResUNet architecture and training setting used for RISING, but we consider $\{(x_{RIS,i}, x_{GT,i})\}_{i=1,\dots,N}$ as training set, imposing the ground truth images as targets (according to the standard LPP philosophy). We denote such reconstructions as x_{LPP} .

5 Experimental results and discussion

In this section, we report and discuss the representative numerical experiments performed using the proposed workflow for tomographic image reconstruction from few-view data.

5.1 Results on the real medical images

Here we present the results of RISING applied to the Mayo data set introduced in paragraph 4.1. As previously mentioned, we consider two sparse-view CT geometries, namely $P_{360,360}$ and $P_{360,180}$. In Figure 4 we report the results for the $P_{360,360}$ protocol, achieved on one image of our test set. The top-left image represents the $x_{RIS} = x^{(15)}$ reconstruction. Even if only a small number of iterations are performed, the main structures of the abdomen are visible; however, the image is still blurry. In the x_{IS} image, shown in the upper-right corner, we notice that the TV regularizer has acted to totally eliminate the artifacts and noise, improving the uniformity of the image in the inner structures. When

compared to the ground-truth solution in Figure 2, the contours of the details in x_{IS} appear slightly jagged, differently from x_{GT} where they are neat but, usually, corrupted by artifacts. The bottom row of Figure 4 shows the two x_{LPP} and x_{ING} images, respectively from left to right. It is evident that x_{LPP} has retrieved many details but it presents noisy components, reflecting the features of its target image x_{GT} . Our solution x_{ING} is less corrupted, since the low-contrast regions are correctly preserved and the noise is not visible. These observations are confirmed by Figure 5, which plots the intensity profiles taken over the red line in the second crop (Figure 2). In our approach (on the right) the CNN has accurately learnt the f map of (8) and the x_{ING} red profile mostly overlaps the black one. On the contrary, the x_{LPP} profile (on the left) is more distant from its target reference.

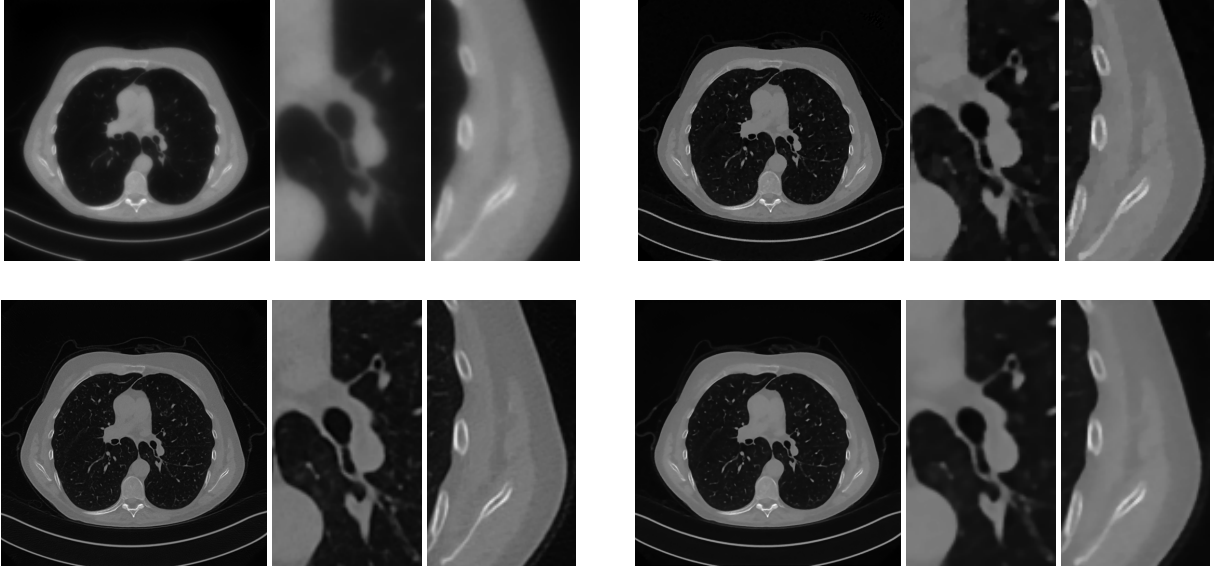


Figure 4: Results on a test image from the Mayo data set, under the $P_{360,360}$ CT protocol. Top-left: x_{RIS} ; top-right: x_{IS} ; bottom-left: x_{LPP} ; bottom-right: x_{ING} .

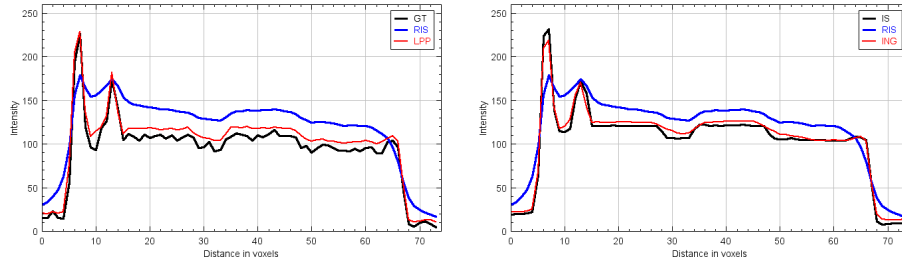


Figure 5: Intensity profiles taken on the horizontal red line depicted in 2, on the reconstructions in Figure 4. Left: the black and red lines are the profile relative to x_{GT} and x_{LPP} respectively. Right: the black and red lines are the profile relative to x_{IS} and x_{ING} respectively. In both the plots, the blue line corresponds to the profile on the starting x_{RIS} image.

We now consider the $P_{180,60}$ CT protocol whose results are reported in Figure 6. In this case, the tomographic reconstruction is more challenging than in the previous experiment. The starting image x_{RIS} has evident streaking artifacts and blur and some details are lost, especially in the first zoom. The artifacts are reduced in the x_{IS} (top right image), where some details are recovered and the edges are quite neat. The x_{ING} image obtained with the proposed RISING (bottom right) is visually an excellent reconstruction. It is very similar to the x_{LPP} image, whose training, we remark, is based on more informative target images.

In Figure 7 we plot for these experiments, the same profiles of Figure 5. In the left graph, we analyse the performance of LPP approach: the x_{LPP} reconstruction gets values quite close to the GT, but it does not fit well the target black line. In the right graph, we analyse the performance of RISING approach: the x_{ING} solution almost overlaps the target x_{IS} profile, confirming that the network has correctly learned.

At last we underline that the solutions of the CS regularized model are very similar in case of $P_{360,360}$ and $P_{180,60}$ geometries.

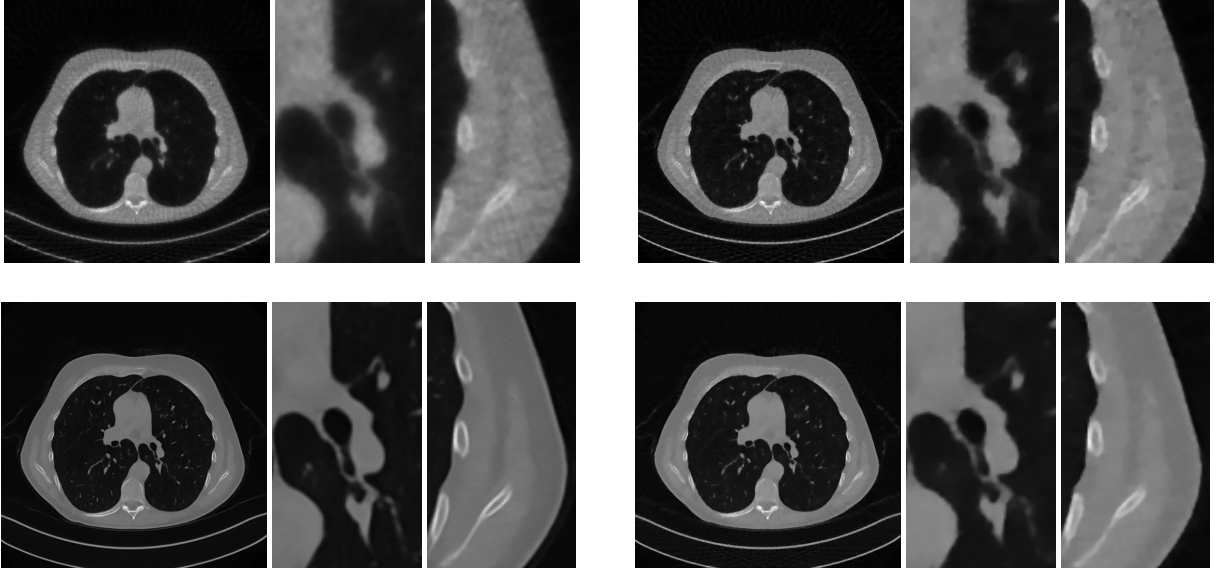


Figure 6: Results on a test image from the Mayo data set, under the $P_{180,60}$ CT protocol. Top-left: x_{RIS} ; top-right: x_{IS} ; bottom-left: x_{LPP} ; bottom-right: x_{ING} .

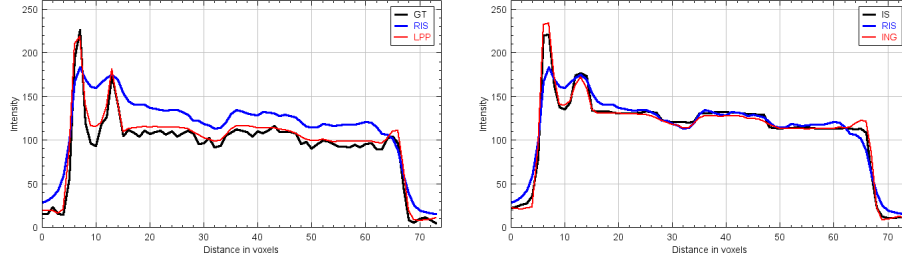


Figure 7: Intensity profiles taken on the horizontal red line depicted in 2, on the reconstructions in Figure 6. Left: the black and red lines are the profile relative to x_{GT} and x_{LPP} respectively. Right: the black and red lines are the profile relative to x_{IS} and x_{ING} respectively. In both the plots, the blue line corresponds to the profile on the starting x_{RIS} image.

5.2 Results on synthetic images

In this paragraph we report the results obtained with RISING on the synthetic COULE data set introduced in paragraph 4.2. Here, the x_{GT} images are digitally created, hence they are not corrupted by noise and artifacts and they can really be used as true images.

5.2.1 Metrics for image quality assessment

To evaluate the efficiency and the accuracy of the reconstructed images, in the following we compute some full-reference image quality assessment metrics. For each considered image x , we consider the relative error (RE) of x with respect to x_{GT} :

$$RE(x) = \frac{\|x - x_{GT}\|_2^2}{\|x_{GT}\|_2^2} \quad (11)$$

and the Root Mean Square Error (RMSE) between x and the reference image y :

$$RMSE(x, y) = \sqrt{\frac{\|x - y\|_2^2}{n^2}} \quad (12)$$

In the following, we set $y = x_{GT}$ unless otherwise stated. We also compute the well-known Structural Similarity (SSIM) index measuring the perceptual difference between two similar images x and y , which is defined as in [40]. In our experiments, we compute the SSIM fixing $y = x_{GT}$.

5.2.2 Analysis for varying rapid reconstructions

As first in-depth analysis, we set the geometry $P_{360,360}$ and we compute the RIS early solutions for $K = \{3, 5, 10\}$. Figure 8 shows the x_{RIS} starting images in the top row and the x_{ING} final reconstructions in the bottom row (relative to the example image of Figure 3). They show that the network in the RIS step is able to almost perfectly learn from all three input images. Figure 9 shows in blue the evolution of the RMSE through the iterations of the SGP for the considered image. In this case $K^* = 58$, i.e. $x_{IS} = x^{(158)}$. The red dots represent the value of the errors of the x_{ING} final reconstructions, for $K = \{3, 5, 10\}$. We observe that the final x_{ING} images are very close to the target x_{IS} , highlighting that the number K of starting iterations seems not to notably influence the final results. In Table 1 we report the analysis on the whole test set, by means of the metrics introduced in the previous paragraph. We observe that the values relative to the x_{ING} solutions are all very similar, independently on K . Moreover, the metrics for the x_{IS} solution show that the image computed by the SGP method well approximates the true one and confirms that the proposed model-based reconstruction algorithm is very efficient.

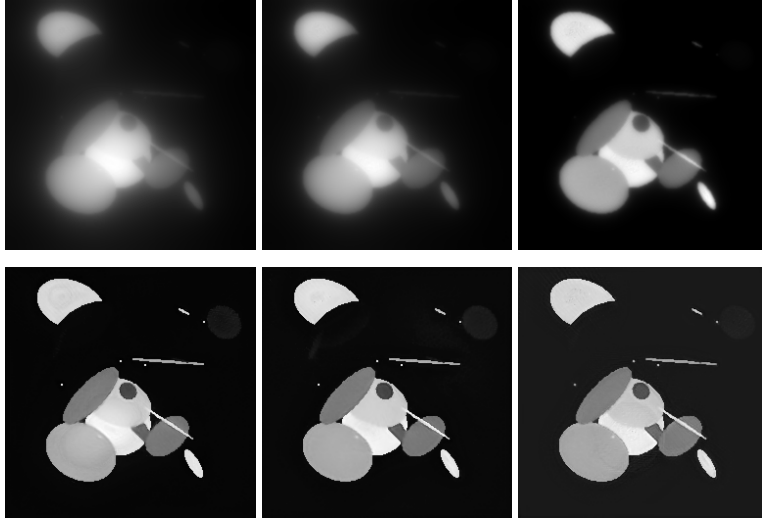


Figure 8: Results on a test image from the COULE synthetic data set, under the $P_{360,360}$ CT protocol. First row, from left to right: x_{RIS} with $K = 3$, $K = 5$ and $K = 10$ respectively; second row, from left to right: the corresponding x_{ING} .

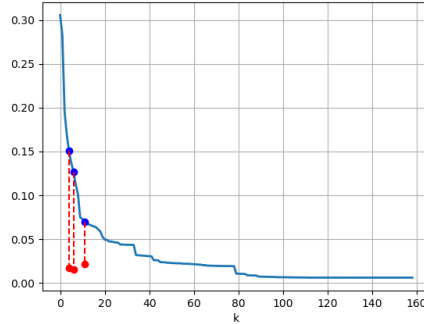


Figure 9: Plot of the RMSE values over the performed iterations, for the reconstruction of an image from the COULE data set, in case of $P_{360,360}$ geometry. The red dots are relative to the x_{ING} images, achieved by the corresponding $x^{(3)}$, $x^{(5)}$ and $x^{(10)}$ RIS images.

Table 1: Mean and standard deviation values of the quality metrics, evaluated on the COULE test set for different RIS reconstructions.

		K=3	K=5	K=10	convergence
RE	x_{RIS}	0.6152 ± 0.0366	0.4996 ± 0.0548	0.2700 ± 0.0239	-
	x_{ING}	0.0681 ± 0.0098	0.0784 ± 0.0844	0.0781 ± 0.0122	-
	x_{IS}	-	-	-	0.0207 ± 0.0051
RMSE	x_{RIS}	0.1768 ± 0.0238	0.1432 ± 0.0218	0.0775 ± 0.0111	-
	x_{ING}	0.0196 ± 0.0042	0.0233 ± 0.0278	0.0225 ± 0.0053	-
	x_{IS}	-	-	-	0.0060 ± 0.0017
SSIM	x_{RIS}	0.2264 ± 0.0262	0.3139 ± 0.0919	0.7844 ± 0.0481	-
	x_{ING}	0.9630 ± 0.0133	0.9267 ± 0.0389	0.9674 ± 0.0140	-
	x_{IS}	-	-	-	0.9980 ± 0.0010

Table 2: Mean and standard deviation values of the quality metrics, evaluated on the COULE test set for different geometries.

		$P_{360,360}$	$P_{360,180}$	$P_{360,60}$
RE	x_{RIS}	0.2700 ± 0.0239	0.2706 ± 0.0240	0.2834 ± 0.0282
	x_{ING}	0.0781 ± 0.0122	0.0676 ± 0.0123	0.1113 ± 0.0223
	x_{IS}	0.0207 ± 0.0051	0.0302 ± 0.0077	0.0668 ± 0.0147
RMSE	x_{RIS}	0.0775 ± 0.0111	0.0777 ± 0.0111	0.0814 ± 0.0123
	x_{ING}	0.0225 ± 0.0053	0.0198 ± 0.0062	0.0318 ± 0.0062
	x_{IS}	0.0060 ± 0.0017	0.0088 ± 0.0026	0.0194 ± 0.0059
SSIM	x_{RIS}	0.7844 ± 0.0481	0.7831 ± 0.0485	0.7472 ± 0.0643
	x_{ING}	0.9674 ± 0.0140	0.9741 ± 0.0115	0.9493 ± 0.0117
	x_{IS}	0.9980 ± 0.0010	0.9951 ± 0.0030	0.9753 ± 0.0141

5.2.3 Analysis for increasing sparsity of the CT subsampling

To understand the behavior of our approach at increasing sparsity in the CT protocol, we also test RISING at different geometric settings such as $P_{360,360}$, $P_{360,180}$ and $P_{360,60}$. The number of iterations used to generate x_{RIS} is $K = 10$ and the K^* iterations needed for convergence is for all the test images in $[150, 300]$. In Table 2 we report the quality indexes evaluated on the test set in terms of mean and standard deviation. We first interestingly observe that the values of all the x_{RIS} outputs are very similar, independently from the geometry. As before, the x_{IS} solutions have excellent metrics, justifying the use of the RISING approach even in the hardest case with only 60 angles. This shows that the considered CS model (5) properly describes the reconstruction process independently of the sparsity of the geometry (at least for the considered ones). Concerning final reconstruction x_{ING} , we see that halving the number of angles in $P_{360,180}$ does not affect the mean values of the metrics; when the geometry is very sparse in $P_{360,60}$ the errors slightly increase. However, the values of the standard deviations are small and very similar in all the tests, showing that the network has a stable behaviour.

5.2.4 Empirical analysis of learnability

In Figure 10 we visualize the error plots of the RMSE values, evaluated as in (12) with $y = x_{IS}$, relative to both the x_{RIS} and x_{ING} images, for all the previously considered settings. We observe that the mean values for the x_{ING} solutions are very small in all the cases. This empirically proves that the neural network has accurately learnt the function f_K in (8), regardless K and the geometry considered. The three very similar RMSE mean values of the x_{RIS} images (for $K = 10$ and different geometries) indicate that, in these experiments, the error decreasing along the SGP iterations does not depend on the sinogram sparsity.

Moreover, we notice that the standard deviation of the RIS images errors are quite high, even if they decrease as K increases. On the contrary, in all the considered experiments, the standard deviations of the ING solutions are extremely small, denoting the stability of the proposed framework when applied to different images.

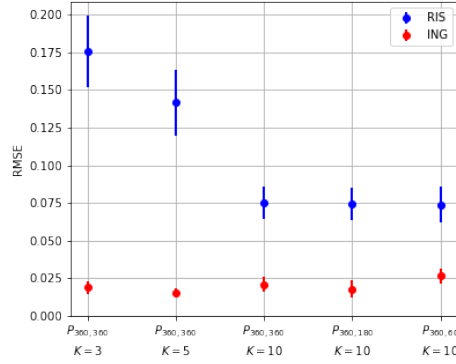


Figure 10: Error plots of the RMSE values, relative to the x_{IS} target images, for the x_{RIS} (in blue) and x_{ING} (in red) reconstructions of the COULE images.

6 Conclusions

We have proposed a novel framework, called RISING, for the reconstruction of a CT image from few-views. RISING uses a Convolutional Neural Network to learn the final iterations of an iterative algorithms solving a gradient-exploiting regularization problem to reconstruct the image from sub-sampled data.

Hence, in RISING the network is trained on a data set obtained by computing the solution of the iterative solver from few-view projections, whereas in the usual LPP schemes the network is trained on *ground truth* images as targets. The numerical experiments performed on a public data set of real abdomen images, the reconstructions are visually very accurate, even in a very sparse geometry with 60 angles in $[0, 180]$ degrees. Surprisingly, in this last case, the RISING network enhances the target image. On a simulated data set of gradient-sparse images, by means of error measures we numerically showed that the RISING framework computes an image very close to the ground truth, which is the desirable solution among the infinite possible of the inverse problems. It is also noticeable that the errors do not depend neither on the iteration considered to get the coarse input image for the network nor on the acquisition geometry.

Finally, we underline that the RISING framework is very flexible, since it can be applied by considering any variational model for computing the inverse problem solution (not limiting to (5)) and/or using other iterative solvers than SGP. In these cases, simply a different function f_K is learned from the network. We also intend to study more theoretical properties, such as some conditions on the iterative methods and on the neural network which guarantee the convergence of the framework solution to the GT image.

References

- [1] Jennifer L Mueller and Samuli Siltanen. *Linear and nonlinear inverse problems with practical applications*. SIAM, 2012.
- [2] Heang K Tuy. An inversion formula for cone-beam reconstruction. *SIAM Journal on Applied Mathematics*, 43(3):546–552, 1983.
- [3] David L Donoho. Compressed sensing. *IEEE Transactions on information theory*, 52(4):1289–1306, 2006.
- [4] C. Graff and E. Sidky. Compressive sensing in medical imaging. *Appl. Opt.*, 54(8):C23–C44, 2015.
- [5] Ge Wang, Jong Chu Ye, Klaus Mueller, and Jeffrey A Fessler. Image reconstruction is a new frontier of machine learning. *IEEE transactions on medical imaging*, 37(6):1289–1296, 2018.
- [6] Yo Seob Han, Jaeyun Yoo, and Jong Chul Ye. Deep residual learning for compressed sensing ct reconstruction via persistent homology analysis. *arXiv preprint arXiv:1611.06391*, 2016.
- [7] Yoseob Han and Jong Chul Ye. Framing u-net via deep convolutional framelets: Application to sparse-view ct. *IEEE transactions on medical imaging*, 37(6):1418–1429, 2018.
- [8] Emil Y Sidky, Iris Lorente, Jovan G Brankov, and Xiaochuan Pan. Do cnns solve the ct inverse problem? *IEEE Transactions on Biomedical Engineering*, 68(6):1799–1810, 2020.

- [9] R Cavicchioli, J Hu, E Loli Piccolomini, E Morotti, and L Zanni. A first-order primal-dual algorithm for convex problems with applications to imaging. GPU acceleration of a model-based iterative method for digital breast tomosynthesis. *Scientific Reports*, 10(1):120–145, 2020. doi:<https://doi.org/10.1038/s41598-019-56920-y>.
- [10] Elena Loli Piccolomini and Elena Morotti. A model-based optimization framework for iterative digital breast tomosynthesis image reconstruction. *Journal of Imaging*, 7(2):36, 2021.
- [11] Avinash C Kak and Malcolm Slaney. *Principles of computerized tomographic imaging*. SIAM, 2001.
- [12] Emmanuel J Candès, Justin Romberg, and Terence Tao. Robust uncertainty principles: Exact signal reconstruction from highly incomplete frequency information. *IEEE Transactions on information theory*, 52(2):489–509, 2006.
- [13] E Loli Piccolomini and E Morotti. A fast total variation-based iterative algorithm for digital breast tomosynthesis image reconstruction. *Journal of Algorithms & Computational Technology*, 10(4):277–289, 2016.
- [14] Qiaofeng Xu, Deshan Yang, Jun Tan, Alex Sawatzky, and Mark A Anastasio. Accelerated fast iterative shrinkage thresholding algorithms for sparsity-regularized cone-beam ct image reconstruction. *Medical physics*, 43(4):1849–1872, 2016.
- [15] Emil Y Sidky, Rick Chartrand, John M Boone, and Xiaochuan Pan. Constrained TpV minimization for enhanced exploitation of gradient sparsity: Application to ct image reconstruction. *IEEE journal of translational engineering in health and medicine*, 2:1–18, 2014.
- [16] Zenith Purisha, Juho Rimpeläinen, Tatiana Bubba, and Samuli Siltanen. Controlled wavelet domain sparsity for x-ray tomography. *Measurement Science and Technology*, 29(1):014002, 2017.
- [17] Vishal Monga, Yuelong Li, and Yonina C Eldar. Algorithm unrolling: Interpretable, efficient deep learning for signal and image processing. *IEEE Signal Processing Magazine*, 38(2):18–44, 2021.
- [18] Ian J. Goodfellow, Yoshua Bengio, and Aaron Courville. *Deep Learning*. MIT Press, Cambridge, MA, USA, 2016. <http://www.deeplearningbook.org>.
- [19] Jonas Adler and Ozan Öktem. Solving ill-posed inverse problems using iterative deep neural networks. *Inverse Problems*, 33(12):124007, 2017.
- [20] Jonas Adler and Ozan Öktem. Learned primal-dual reconstruction. *IEEE transactions on medical imaging*, 37(6):1322–1332, 2018.
- [21] Harshit Gupta, Kyong Hwan Jin, Ha Q Nguyen, Michael T McCann, and Michael Unser. Cnn-based projected gradient descent for consistent ct image reconstruction. *IEEE transactions on medical imaging*, 37(6):1440–1453, 2018.
- [22] Jinxi Xiang, Yonggui Dong, and Yunjie Yang. Fista-net: Learning a fast iterative shrinkage thresholding network for inverse problems in imaging. *IEEE Transactions on Medical Imaging*, 40(5):1329–1339, 2021. doi:10.1109/TMI.2021.3054167.
- [23] Haimiao Zhang, Baodong Liu, Hengyong Yu, and Bin Dong. Metainv-net: Meta inversion network for sparse view ct image reconstruction. *IEEE Transactions on Medical Imaging*, 40(2):621–634, 2020.
- [24] Daniël M Pelt, Kees Joost Batenburg, and James A Sethian. Improving tomographic reconstruction from limited data using mixed-scale dense convolutional neural networks. *Journal of Imaging*, 4(11):128, 2018.
- [25] Tao Zhang, Hwei Gao, Yuxiang Xing, Zhiqiang Chen, and Li Zhang. Dualres-unet: Limited angle artifact reduction for computed tomography. In *2019 IEEE Nuclear Science Symposium and Medical Imaging Conference (NSS/MIC)*, pages 1–3. IEEE, 2019.
- [26] Alena-Kathrin Schnurr, Khanlian Chung, Tom Russ, Lothar R Schad, and Frank G Zöllner. Simulation-based deep artifact correction with convolutional neural networks for limited angle artifacts. *Zeitschrift für Medizinische Physik*, 29(2):150–161, 2019.
- [27] Yasuyo Urase, Mizuho Nishio, Yoshiko Ueno, Atsushi K Kono, Keitaro Sofue, Tomonori Kanda, Takaki Maeda, Munenobu Nogami, Masatoshi Hori, and Takamichi Murakami. Simulation study of low-dose sparse-sampling ct with deep learning-based reconstruction: usefulness for evaluation of ovarian cancer metastasis. *Applied Sciences*, 10(13):4446, 2020.
- [28] Elena Morotti, Davide Evangelista, and Elena Loli Piccolomini. A green prospective for learned post-processing in sparse-view tomographic reconstruction. *Journal of Imaging*, 7(8):139, 2021.
- [29] Tatiana A Bubba, Gitta Kutyniok, Matti Lassas, Maximilian Maerz, Wojciech Samek, Samuli Siltanen, and Vignesh Srinivasan. Learning the invisible: a hybrid deep learning-shearlet framework for limited angle computed tomography. *Inverse Problems*, 35(6):064002, 2019.

- [30] Zhuoran Jiang, Yingxuan Chen, Yawei Zhang, Yun Ge, Fang-Fang Yin, and Lei Ren. Augmentation of cbct reconstructed from under-sampled projections using deep learning. *IEEE transactions on medical imaging*, 38(11):2705–2715, 2019.
- [31] Leonid I. Rudin, Stanley Osher, and Emad Fatemi. Nonlinear total variation based noise removal algorithms. *Physica D: Nonlinear Phenomena*, 60(1):259 – 268, 1992. URL: <http://www.sciencedirect.com/science/article/pii/016727899290242F>, doi:[https://doi.org/10.1016/0167-2789\(92\)90242-F](https://doi.org/10.1016/0167-2789(92)90242-F).
- [32] Silvia Bonettini, Riccardo Zanella, and Luca Zanni. A scaled gradient projection method for constrained image deblurring. *Inverse problems*, 25(1):015002, 2008.
- [33] Elena Loli Piccolomini, V.L. Coli, E. Morotti, and L. Zanni. Reconstruction of 3D X-ray CT images from reduced sampling by a scaled gradient projection algorithm. *Comp. Opt. Appl.*, 71:171–191, 2018. doi:<https://doi.org/10.1007/s10589-017-9961-2>.
- [34] S Bonettini, F Porta, and V Ruggiero. A variable metric inertial method for convex optimization. *SIAM J. Sci. Comput.*, 31(4):A2558–A2584, 2016.
- [35] C McCollough. Tu-fg-207a-04: Overview of the low dose ct grand challenge. *Medical physics*, 43(6Part35):3759–3760, 2016.
- [36] Olaf Ronneberger, Philipp Fischer, and Thomas Brox. U-net: Convolutional networks for biomedical image segmentation. In *International Conference on Medical image computing and computer-assisted intervention*, pages 234–241. Springer, 2015.
- [37] Jong Chul Ye, Yoseob Han, and Eunju Cha. Deep convolutional framelets: A general deep learning framework for inverse problems. *SIAM Journal on Imaging Sciences*, 11(2):991–1048, 2018.
- [38] Wim van Aarle, Willem Jan Palenstijn, Jan De Beenhouwer, Thomas Altantzis, Sara Bals, K. Joost Batenburg, and Jan Sijbers. The astra toolbox: A platform for advanced algorithm development in electron tomography. *Ultramicroscopy*, 157:35–47, 2015. URL: <https://www.sciencedirect.com/science/article/pii/S0304399115001060>, doi:<https://doi.org/10.1016/j.ultramic.2015.05.002>.
- [39] Wim van Aarle, Willem Jan Palenstijn, Jeroen Cant, Eline Janssens, Folkert Bleichrodt, Andrei Dabrovolski, Jan De Beenhouwer, K. Joost Batenburg, and Jan Sijbers. Fast and flexible x-ray tomography using the astra toolbox. *Opt. Express*, 24(22):25129–25147, Oct 2016. URL: <http://www.osapublishing.org/oe/abstract.cfm?URI=oe-24-22-25129>, doi:10.1364/OE.24.025129.
- [40] Zhou Wang, Alan C Bovik, Hamid R Sheikh, and Eero P Simoncelli. Image quality assessment: from error visibility to structural similarity. *IEEE transactions on image processing*, 13(4):600–612, 2004.